Inorg. Chem. **2008**, *47*, 8077−8085

$CaMn_{1-x}Nb_xO_3$ ($x \leq 0.08$) Perovskite-Type Phases As Promising New High-Temperature *n*-Type Thermoelectric Materials

L. Bocher, M. H. Aguirre, D. Logvinovich, A. Shkabko, R. Robert, M. Trottmann, and A. Weidenkaff*

Empa - Solid State Chemistry and Catalysis, Ueberlandstrasse 129, Duebendorf CH-8600, Switzerland

Received March 13, 2008

Perovskite-type $CaMn_{1-x}Nb_xO_{3\pm\delta}$ ($x = 0.02$, 0.05, and 0.08) compounds were synthesized by applying both a "chimie douce" (SC) synthesis and a classical solid state reaction (SSR) method. The crystallographic parameters of the resulting phases were determined from X-ray, electron, and neutron diffraction data. The manganese oxidations states (Mn^{4+}/Mn^{3+}) were investigated by X-ray photoemission spectroscopy. The orthorhombic $CaMn_{1-x}Nb_xO_{3\pm\delta}$ ($x = 0.02$, 0.05, and 0.08) phases were studied in terms of their high-temperature thermoelectric properties (Seebeck coefficient, electrical resistivity, and thermal conductivity). Differences in electrical transport and thermal properties can be correlated with different microstructures obtained by the two synthesis methods. In the high-temperature range, the electron-doped manganate phases exhibit large absolute Seebeck coefficient and low electrical resistivity values, resulting in a high power factor, PF (e.g., for $x = 0.05$, $S_{1000K} = -180\ \mu V\ K^{-1}$, $\rho_{1000K} = 16.8\ m\Omega$ cm, and PF > 1.90×10^{-4} W m^{-1} K^{-2} for 450 K < T < 1070 K). Furthermore, lower thermal conductivity values are achieved for the SC-derived phases (κ < 1 W m^{-1} K^{-1}) compared to the SSR compounds. High power factors combined with low thermal conductivity (leading to ZT values > 0.3) make these phases the best perovskitic candidates as *n*-type polycrystalline thermoelectric materials operating in air at high temperatures.

Introduction

Thermoelectric (TE) applications turn out nowadays to be a potential technology to enable the direct conversion of heat into electric power.[1] This energy conversion has the advantage of being maintenance-free, since electricity is generated (i) without involvement of chemical reactions compared to solid oxide fuel cell devices[2] and (ii) without operation of moving parts, unlike the gas turbine engines.

The efficient conversion of heat into electricity requires the development of functional materials with a high figure of merit, $Z = S^2/\rho\kappa$.[3] In this respect, complex metal oxides have proven to be promising TE candidates, especially layered cobaltate structures, i.e., Na_xCoO_2[4] and $Ca_3Co_4O_9$[5] as well as perovskite-type phases, with the general formula ABO_3. Perovskite-type phases have very attractive physical−chemical properties coupled with a flexible crystal structure. Thus, properties of perovskites can be modified and fine-tuned in a controlled way by cationic substitutions and changes in oxygen content.[6,7] Increased Seebeck coefficients, S, combined with decreased electrical resistivity, ρ, can be accomplished by slight cationic or anionic substitutions in these materials.[8,9] The challenge is to concurrently reduce the thermal conductivity, κ, defined as the sum of an electronic and a lattice component (κ_e and κ_l, respectively).[10,11] In oxide materials κ_l prevails since phonons are the predominant heat carriers. Therefore, different strategies

* Author to whom correspondence should be addressed. E-mail: anke.weidenkaff@empa.ch.

(1) Funahashi, R.; Urata, S. *Int. J. Appl. Ceram. Technol.* **2007**, *4*, 297.
(2) Boudghene Stambouli, A.; Traversa, E. *Renewable Sustainable Energy Rev.* **2002**, *6*, 433–455.
(3) Rowe, D. M. *Thermoelectrics Handbook - Macro to Nano*; CRC Press/Taylor & Francis Group: Boca Raton, FL, 2006.
(4) Terasaki, I.; Sasago, Y.; Uchinokura, K. *Phys. Rev. B: Condens. Matter Mater. Phys.* **1997**, *56*, R12685–R12687.
(5) Masset, A. C.; Michel, C.; Maignan, A.; Hervieu, M.; Toulemonde, O.; Studer, F.; Raveau, B.; Hejtmanek, J. *Phys. Rev. B: Condens. Matter Mater. Phys.* **2000**, *62*, 166–175.
(6) Galasso, F. S. *Structure, Properties and Preparation of Perovskite-type Compounds*; Pergamon Press Ltd.: Oxford, U.K., 1969.
(7) Raveau, B. *Prog. Solid State Chem.* **2007**, *35*, 171–173.
(8) Maignan, A.; Martin, C.; Damay, F.; Raveau, B. *Phys. Rev. B: Condens. Matter Mater. Phys.* **1998**, *58*, 2758–2763.
(9) Logvinovich, D.; Aguiar, R.; Robert, R.; Trottmann, M.; Ebbinghaus, S.; Reller, A.; Weidenkaff, A. *J. Solid State Chem.* **2007**, *180*, 2649–2654.
(10) Tritt, T. M. *Theory, Thermal Conductivity - Theory, Properties and Applications*; Kluwer Academic/Plenum Publishers: New York, 2004.
(11) Kittel, Ch. *Introduction to Solid State Physics*, 8th ed.; John Wiley Sons, Inc: New York, 2004.

10.1021/ic800463s CCC: $40.75
Published on Web 08/13/2008

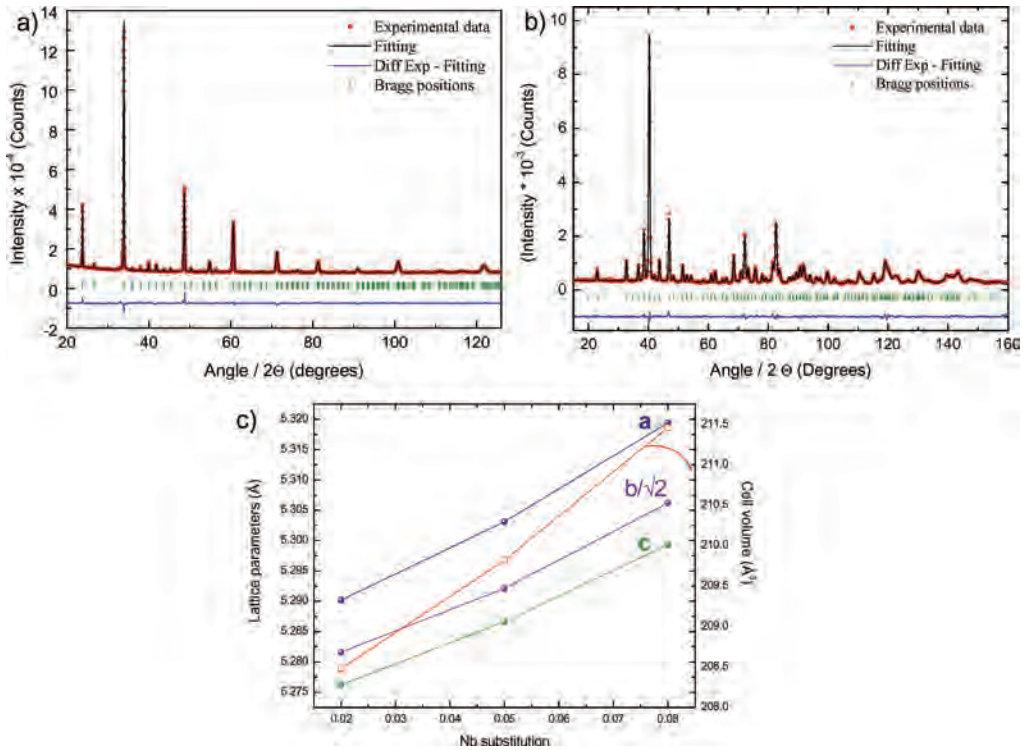

Figure 1. Examples of Rietveld refinements from (a) the XRPD data of $CaMn_{0.95}Nb_{0.05}O_3$, (b) the neutron diffraction data of $CaMn_{0.92}Nb_{0.08}O_3$ recorded at 300 K, and (c) lattice parameters and cell volumes of the $CaMn_{1-x}Nb_xO_3$ series ($x \leq 0.10$) as a function of the Nb substitution, derived from neutron diffraction data.

to lower the lattice heat conduction by phonon scattering are pursued. Phonon scattering may be promoted by complex crystal structures (e.g., perovskite structures) with several atoms per unit cell, by nanometer-sized crystallites due to an increasing amount of grain boundaries[12] and by the introduction of foreign atoms acting as additional scattering centers.[10,13] In addition, oxide materials are cost-efficient and nontoxic compared to conventional TE tellurite-based compounds. They are also chemically and thermally stable at high temperatures in oxidative atmospheres.

Perovskite-type phases such as, for example, manganate,[14] titanate,[15] or cobaltate[16] phases reveal large Seebeck coefficients, one of the essential prerequisites for potential TE materials. The large thermopower values are caused by a strong interplay between charge, electron spin states, and crystal structure.[8,17−19] In particular, electron-doped manganates show promising thermoelectric properties at elevated temperatures ($T \gg 300$ K).[15,20−27] Perovskite-type manganate phases are already widely studied due to their colossal magnetoresistance,[28−30] which is explained by the double exchange (DE) model.[31] Since the antiferromagnetic insulator $CaMnO_3$ exhibits large absolute thermopower values,[8] appropriate substitutions at the A or B site increase the

Table 1. Refined Structural Parameters, Atomic Positions of the $CaMn_{1-x}Nb_xO_3$ series ($x = 0.02, 0.05, 0.08$) from Neutron Diffraction Data Obtained at 298 K[a]

composition		$CaMn_{0.98}Nb_{0.02}O_3$	$CaMn_{0.95}Nb_{0.05}O_3$	$CaMn_{0.92}Nb_{0.08}O_3$
a (Å)		5.2902 (1)	5.3031 (2)	5.3194 (2)
b (Å)		7.4693 (1)	7.4842 (2)	7.5041 (3)
c (Å)		5.2762 (1)	5.2866 (2)	5.2975 (2)
V (Å^3)		208.48	209.82	211.46
Ca	x	0.0327 (5)	0.0324 (6)	0.0319 (6)
	y	0.25	0.25	0.25
	z	−0.0064 (8)	−0.0073 (10)	−0.0070 (11)
	biso (Å^2)	0.84 (4)	0.88 (4)	1.03 (4)
	occupancy	0.5	0.5	0.5
Mn/Nb	x	0	0	0
	y	0	0	0
	z	0.5	0.5	0.5
	biso (Å^2)	0.44 (4)	0.57 (4)	0.73(6)
	occupancy	0.49/0.01	0.475/0.025	0.46/0.04
O_{ap}	x	0.4896 (5)	0.4891 (5)	0.4880 (6)
	y	0.25	0.25	0.25
	z	0.0679 (7)	0.0678(6)	0.0660 (7)
	biso (Å^2)	0.66 (7)	0.73(3)	0.96 (4)
	occupancy	0.5	0.5	0.5
O_{eq}	x	0.2866 (4)	0.2873 (3)	0.2880 (4)
	y	0.0337 (2)	0.0333 (3)	0.0342 (3)
	z	0.7129 (4)	0.7127 (3)	0.7132 (4)
	biso (Å^2)	0.70 (4)	0.73 (2)	0.94 (2)
	occupancy	1	1	1
R_{wp}		9.01	9.02	10
R_p		8.44	9.21	9.65
χ^2		1.47	1.78	1.37

[a] Atoms are located at the following Wyckoff position: Ca, 4(c); Mn/Nb, 4(b); Oap, 4(c); and Oeq, 8(d).

(12) Hicks, L. D.; Dresselhaus, M. S. *Phys. Rev. B: Condens. Matter Mater. Phys.* **1993**, *47*, 12727–12731.
(13) Winter, M. R.; Clarke, D. R. *J. Am. Ceram. Soc.* **2007**, *90*, 533–540.
(14) Bocher, L.; Robert, R.; Aguirre, M. H.; Malo, S.; Hebert, S.; Maignan, A.; Weidenkaff, A. *Solid State Sci.* **2008**, *10*, 496−501.
(15) Ohta, S.; Ohta, H.; Koumoto, K. *J. Ceram. Soc. Jpn.* **2006**, *114*, 102–105.
(16) Robert, R.; Bocher, L.; Sipos, B.; Döbeli, M.; Weidenkaff, A. *Prog. Solid State Chem.* **2007**, *35*, 447–455.
(17) Hejtmánek, J.; Jirák, Z.; Marysko, M.; Martin, C.; Maignan, A.; Hervieu, M.; Raveau, B. *Phys. Rev. B: Condens. Matter Mater. Phys.* **1999**, *60*, 14057–14065.
(18) Hébert, S.; Flahaut, D.; Martin, C.; Lemonnier, S.; Noudem, J.; Goupil, C.; Maignan, A. *Prog. Solid State Chem.* **2007**, *35*, 457–467.
(19) Kobayashi, W.; Terasaki, I.; Mikami, M.; Runahashi, R.; Nomura, T.; Katsufuji, T. *J. Appl. Phys.* **2004**, *95*, 6825–6827.

Table 2. Tolerance and Orthorhombicity Factors, Bond Distances and Distortion Angles of the $CaMn_{1-x}Nb_xO_3$ Series ($x = 0.02, 0.05, 0.08$) from Neutron Diffraction Data

composition	$CaMn_{0.98}Nb_{0.02}O_3$	$CaMn_{0.95}Nb_{0.05}O_3$	$CaMn_{0.92}Nb_{0.08}O_3$
tolerance factor: t^a	1.0005	0.99549	0.99052
orthorhombicity factor: a/c	1.0026	1.0031	1.0041
Mn−O_{ap} × 2 (Å)	1.9022 (7)	1.9059 (6)	1.9094 (7)
Mn−O_{eq1} × 2 (Å)	1.9040 (2)	1.9099 (16)	1.9210 (2)
Mn−O_{eq2} × 2 (Å)	1.9060 (2)	1.9082 (16)	1.9090 (2)
Mn−O_{ap}−Mn (deg)	158.03 (3)	158.04 (3)	158.54 (3)
Mn−O_{eq}−Mn (deg)	157.41 (9)	157.38 (7)	157.09 (9)

[a] The Goldsmith tolerance factor, t, for the perovskite structure ABO_3 is defined by $t \approx (r_A + r_O)/\sqrt{2}(r_B + r_O)$.

concentration of charge carriers. Hence, the introduction of Nb^{5+} on the B site leads to the formation of Mn^{3+} in the Mn^{4+} matrix, which corresponds to electron doping in the e_g band.[32,33] This substituted manganate phase has a lower electrical resistivity compared to $CaMnO_3$ and can be modeled as a DE system coupled to the Jahn−Teller cation Mn^{3+}.[8]

While comprehensive studies are available on the improvement of transport properties, the thermal conduction behavior of complex metal oxides has not been intensively investigated so far. A reduction of the thermal conductivity, $\kappa(T)$, might be achieved without affecting the power factor by adjusting the particle morphology and microstructure. In the present paper, the differences in morphology and microstructure of $CaMn_{1-x}Nb_xO_{3\pm\delta}$ compounds ($x = 0.02$, 0.05, and 0.08) depending on the applied synthesis method are determined. The synthesized electron-doped manganate phases are studied in view of a correlation between their morphological characteristics and their TE parameters S, ρ, and κ.

Experimental Section

Polycrystalline perovskite-type phases of $CaMn_{1-x}Nb_xO_3$ (with $x = 0.02$, 0.05, and 0.08) were synthesized by a "chimie douce" synthesis method (abbreviated SC for soft chemistry method) with particular attention to low synthesis temperatures (873 K < T < 1073 K).[16,34,35] The implemented SC method consisted of the preparation of complex precursors, which were subsequently decomposed by stepwise calcination. Additionally, a classical solid-state reaction method (SSR) was used to prepare ceramic samples with the same composition.

For the SC method, the required amounts of $Ca(NO_3)_2 \cdot 4H_2O$ (Fluka; ≥ 99%) and $Mn(NO_3)_2 \cdot 4H_2O$ (Merck; > 98.5%) were dissolved in deionized water. Citric acid ($C_6H_8O_7$, Riedel-de Häen; > 99.5%) was used as chelating agent and added in excess with a citric acid/metal cation molar ratio of 2:1 in order to prevent precipitation and $NbCl_5$ hydrolysis. $NbCl_5$ (Aldrich; > 99.5%) was added to the solution after prior dissolution in hydrochloric acid. A 0.5 M precursor solution was obtained by homogenization and subsequent polymerization at 353 K for 3 h under continuous stirring. No precipitation was observed, which indicates the formation of water-soluble polymeric complex compounds. The obtained xerogel precursor was heated in air at a rate of 20 K/h to a final temperature of 573 K and maintained at this temperature for another 3 h. After intermediate grinding, the ashlike powder was calcined at 1073 K for 6 h. The resultant powders were pressed into discs or bars and sintered in air at 1473 K for 5 h. For the SSR method, stoichiometric amounts of $CaCO_3$ (Alfa Aesar; > 99.5%), MnO_2 (Specpure), and Nb_2O_5 (Specpure) were thoroughly mixed in ethanol. The mixtures were pressed as described previously and sintered in air at 1673 K for 6 h, including several intermediate grindings, yielding polycrystalline oxide powders.

The phase purity was studied by X-ray powder diffraction (XRPD) using a Phillips X'Pert PRO MPD Θ-Θ System equipped with a linear detector X'Celerator. Crystallographic parameters were obtained from Rietveld refinements of the neutron diffraction (ND) data collected at $T = 298$ K. The ND data were recorded with a high-resolution powder diffractometer for thermal neutrons[36] located at the Swiss Spallation Neutron Source in the Paul Scherrer Institute (Switzerland). Samples were placed in cylindrical vanadium cans of 8 mm in diameter. The measurements were performed with a neutron wavelength of $\lambda = 1.494$ Å in an angular range of 4.5−165° with a step size of 0.05°. The instrument was operating in a high-intensity mode. The reflection shape was modeled by a Thompson−Cox−Hastings (TCH) pseudo-Voigt profile function[37] corrected for asymmetry[38,39] and the background by a 12-coefficient polynomial function. Rietveld refinements were performed using the FULL-PROF program.[40,41] Electron diffraction (ED) and high-resolution transmission electron microscopy (HRTEM) studies were carried out using a Philips CM30 electron microscope. TEM samples were prepared by dispersion of ground powders in ethanol and deposition on a holey carbon film. The morphology of the sintered pellets was investigated by scanning electron microscopy (SEM) using a Hitachi FEG-SEM S4700. The cationic composition of randomly selected particles was analyzed by energy dispersive X-ray spectroscopy (EDS) coupled to SEM. Results of independent EDS determinations were averaged. X-ray photoemission spectroscopy

(20) Kobayashi, T.; Takizawa, H.; Endo, T.; Sato, T.; Shimada, M. *J. Solid State Chem.* **1991**, *92*, 116–129.
(21) Ohtaki, M.; Koga, H.; Tokunaga, T.; Eguchi, K.; Arai, H. *J. Solid State Chem.* **1995**, *120*, 105–111.
(22) Pi, L.; Martin, C.; Maignan, A.; Raveau, B. *Phys. Rev. B: Condens. Matter Mater. Phys.* **2003**, *67*, 1–7024430.
(23) Thao, P. X.; Tsuji, T.; Hashida, M.; Yamamura, Y. *J. Ceram. Soc. Jpn.* **2003**, *111*, 544–547.
(24) Cong, B. T.; Tsuji, T.; Thao, P. X.; Thanh, P. Q.; Yamamura, Y. *Physica B* **2004**, *352*, 18–23.
(25) Xu, G.; Funahashi, R.; Pu, Q.; Liu, B.; Tao, R.; Wang, G.; Ding, Z. *Solid State Ionics* **2004**, *171*, 147–151.
(26) Miclau, M.; Hébert, S.; Retoux, R.; Martin, C. *J. Solid State Chem.* **2005**, *178*, 1104–1111.
(27) Flahaut, D.; Mihara, T.; Funahashi, R.; Nabeshima, N.; Lee, K.; Ohta, H.; Koumoto, K. *J. Appl. Phys.* **2006**, *100*, 1–4084911.
(28) von Helmolt, R.; Wecker, J.; Holzapfel, B.; Schultz, L.; Samwer, K. *Phys. Rev. Lett.* **1993**, *71*, 2331.
(29) Urishibara, A.; Moritomo, Y.; Avima, T.; Asamitsu, A.; Kido, G.; Tokura, Y. *Phys. Rev. B: Condens. Matter Mater. Phys.* **1995**, *51*, 14103-
(30) Rao, C. N. R.; Raveau, B. *Colossal Magnetoresistance*; World Scientific: Singapore, 1998.
(31) Zener, C. *Phys. Rev.* **1951**, *82*, 403–405.
(32) Raveau, B.; Zhao, Y. M.; Martin, C.; Hervieu, M.; Maignan, A. *J. Solid State Chem.* **2000**, *149*, 203–207.
(33) Goodenough, J. B.; Wold, A.; Arnott, R. J.; Menwuik, N. *Phys. Rev.* **1961**, *124*, 373–384.
(34) Weidenkaff, A. *Adv. Eng. Mater.* **2004**, *9*, 709–714.
(35) Bocher, L.; Aguirre, M. H.; Robert, R.; Trottmann, M.; Logvinovich, D.; Hug, P.; Weidenkaff, A. *Thermochim. Acta* **2007**, *457*, 11–19.
(36) Fischer, P.; Frey, G.; Koch, M.; Konnecke, M.; Pomjakushin, V.; Schefer, J.; Thut, R.; Schlumpf, N.; Burge, R.; Greuter, U. *Physica B* **2000**, *276−278*, 146–147.
(37) Thompson, P.; Cox, D. E.; Hastings, J. B. *J. Appl. Crystallogr.* **1987**, *20*, 79–83.
(38) van Laar, B.; Yelon, W. B. *J. Appl. Crystallogr.* **1984**, *17*, 47–54.
(39) Finger, L. W.; Cox, D. E.; Jephcoat, A. P. *J. Appl. Crystallogr.* **1994**, *27*, 892–900.
(40) Rodriguez-Carvajal, J. *Physica B* **1993**, *192*, 55–69.
(41) Rietveld, H. M. *J. Appl. Cryst.* **1969**, *2*, 65–71.

Table 3. B-Site Cationic Composition and Oxygen Content for the $CaMn_{1-x}Nb_xO_{3+\delta}$ Series ($x = 0.02, 0.05, 0.08$)

synthesis method	niobium substitution	cationic composition		oxygen content
		Mn	Nb	
SC	0.02	0.98 ± 0.01	0.013 ± 0.075	3.07 ± 0.05
	0.05	0.95 ± 0.01	0.047 ± 0.030	3.06 ± 0.07
	0.08	0.92 ± 0.01	0.079 ± 0.015	3.04 ± 0.05
SSR	0.02	0.98 ± 0.02	0.015 ± 0.070	3.03 ± 0.06
	0.05	0.95 ± 0.02	0.049 ± 0.040	3.08 ± 0.06
	0.08	0.93 ± 0.02	0.069 ± 0.020	3.09 ± 0.05

(XPS) measurements were performed on a PHI Quantum 2000 spectrometer using monochromatic Al Kα X-rays (1486.6 eV). The hemispherical energy analyzer was operated at constant pass energy of 58.7 eV and a resolution of 0.25 eV. Prior to the measurements, the sintered SC samples were sputtered for 120 s, causing a decrease in thickness of approximately 10−20 nm. The sample charge was neutralized with electron flood and ion guns. XPS spectra were recorded at room temperature at a photoelectron takeoff angle of 45° with respect to the surface plane. The background was subtracted using the Shirley method, and all spectra were referenced to the O 1s line at 530 eV.[42] The oxygen content was determined by reduction experiments using a Netzsch STA 409 CD thermogravimetric analysis (TGA). The polycrystalline compounds were heated up to 1173 K at a rate of 10 K/min under a reducing atmosphere (20% vol H_2/He), leading to the formation of $CaMnO_2$, according to $CaMnO_3$ (s) + H_2 (g) at 1173 K → $CaMnO_2$ (s) + 1/2 O_2.[43]

The resistivity and TEP measurements were carried out on a bar-shaped sample ($1.5 \times 1 \times 5$ mm^3) between 320 and 1070 K in ambient air using a RZ2001i unit from Ozawa Science (Japan). The detailed experimental procedure is described elsewhere.[15] The high-temperature thermal conductivity, κ, was determined from measurements of the thermal diffusivity, α, the heat capacitiy, Cp, and the density, d, using the relationship: $\kappa = d \times \alpha \times Cp$. The relative bulk density was measured by the Archimedes method, reflecting the open porosity of the samples. The thermal diffusivity of a disk-shaped sample (approximately 1 mm thickness × 10 mm diameter) was determined in air between 300 and 1070 K with a heating rate of 5 K/min, using a Netzsch LFA 457 laser flash apparatus. This instrument uses a solid-state laser ($\lambda = 1064$ nm) to heat one side of the polycrystalline sample and an InSb infrared detector to measure the corresponding heat increase on the back side. The method is based on the laser flash technique invented by Parker et al.[44] The specific heat was determined by differential scanning calorimetry (DSC) using a Netzsch DSC 404 C Pegasus. The polycrystalline sample was heated from room temperature to 1070 K at a heating rate of 20 K/min under a synthetic air atmosphere (20% vol O_2/He) with a gas flow rate of 50 mL/min. Three experiments were performed successively to determine the specific heat by the ratio method: (a) the baseline, (b) the standard sample with a known Cp (sapphire), and (c) the polycrystalline sample.

Results and Discussions

The XRPD data (Figure 1a) confirm the single-phase nature of the synthesized compounds. The refined structural parameters, atomic positions and agreement factors from the ND data are summarized in Table 1. The reflections can be indexed in the orthorhombic type structure (Figure 1b), *Pnma* space group with the cell parameters $\sim a_p\sqrt{2} \times 2a_p \times a_p\sqrt{2}$, corresponding to the $a^+b^-b^-$ type tilting ($a_p \sim 3.74$ Å refers to the lattice parameter for the ideal cubic perovskite structure). Figure 1c shows the evolution of the lattice parameters and cell volume with increased Nb substitution. The B-site Nb substitution causes an increasing of the lattice parameters and cell volume, as previously reported.[25] This evolution can be explained by the larger ionic radii of both cations Nb^{5+} and Mn^{3+}, generated in the Mn^{4+} matrix (ionic radii of Mn^{4+}, Mn^{3+}, and Nb^{5+} are 0.530, 0.645, and 0.740 Å, respectively[45]). The following relation is observed: $c < b/\sqrt{2} < a$, indicating an O-type orthorhombic deformation for the $CaMn_{1-x}Nb_xO_3$ (with $x \leq 0.08$) phases. The orthorhombic distortions, characterized by the Mn−O apical and equatorial distances and the distortion angles (Mn−O_{ap}−Mn and Mn−O_{eq}−Mn), are listed in Table 2 along with the Goldsmith tolerance and orthorhombicity factors. The tolerance factor, t, represents a structural parameter describing geometrical distortion, with $t = 1$ denoting an ideal perovskite structure. For the studied phases, a decrease in the tolerance factor with increasing Nb substitution was observed, indicating that the octahedral distortion is enhanced in this structure. This distortion of the BO_6 octahedra is also confirmed by the simultaneous increase of the orthorhombicity factor and the fact that the measured Mn−O−Mn angles are not equal to 180°.

The compositions of all of the synthesized compounds are listed in Table 3. Thermogravimetric reduction experiments show a slight oxygen excess for all phases, leading to values of $\delta \leq 0.9$. Since in the perovskite-type manganate phases generally no additional oxygen sites can be generated, this finding is considered as representing cation vacancies rather than oxygen excess.[46] The cationic compositions of the compounds are in good agreement with the intended compositions, except for the SSR phase with 8% Nb substitution, where the EDX results suggest a lower Nb content than expected (see Table 3). In addition, it can be stated that the error range of the EDX evaluations is higher for Nb (with contents $x < 0.10$) compared to the main elements, that is, manganese. It is well-known that, in SC processes, the cations of the perovskite phase are mixed in liquid solution, while in conventional ceramic methods, the interdiffusion of the

(42) Moulder, J. F.; Stickle, W. F.; Sobol, P. E.; Bomben, K. D. *Handbook of X-ray Photoelectron Spectroscopy*; Physical Electronics Inc: Chanhassen, MN, 1995.
(43) Poeppelmeier, K. R.; Leonowicz, M. E.; Longo, J. M. *J. Solid State Chem.* **1982**, *44*, 89–98.
(44) Parker, W. J.; Jenkins, R. J.; Butler, C. P.; Abbott, G. L. *J. Appl. Phys.* **1961**, *32*, 1679–1684.
(45) Shannon, R. D. *Acta Crystallogr, Sect. A* **1976**, *32*, 751–767.
(46) Töpfer, J.; Goodenough, J. B. *J. Solid State Chem.* **1997**, *130*, 117–128.

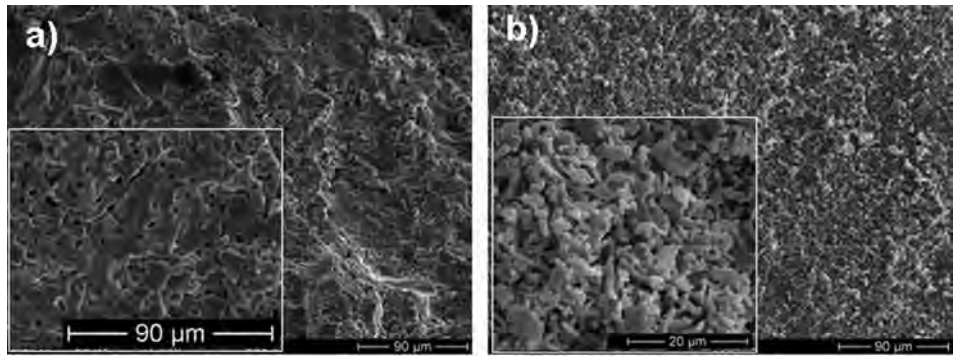

Figure 2. SEM pictures of $CaMn_{0.95}Nb_{0.05}O_3$ cross-section sintered pellets synthesized by the (a) SSR method and (b) SC method. (The bulk relative densities of the SC and SSR compounds are respectively equal to $d_{SSR} \simeq 82.90\%$ and $d_{SC} \simeq 67.70\%$.)

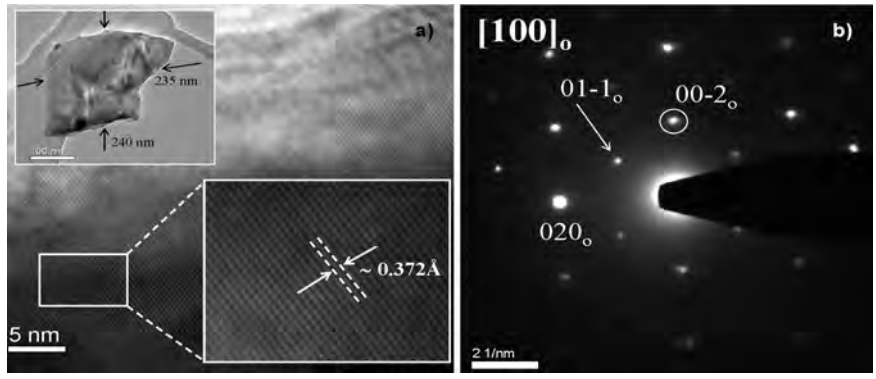

Figure 3. (a) HRTEM and (b) ED of $CaMn_{0.98}Nb_{0.02}O_3$ (prepared by SC synthesis) in the $[100]_o$ zone axis. The inset in a presents a low-resolution TEM image of the studied crystallite.

cations in a solid matrix is necessary to homogenize the product phases.[34] Thus, small concentrations of Nb can be fast and homogeneously distributed in the Ca−Mn mixture by using citric acid as a chelating agent for all cations in the aqueous solution.

Figure 2a and b exhibit the typical particle morphology of sintered pellets obtained by the SSR and the SC synthesis methods, respectively. Grains of 3−10 μm size are achieved for SSR phases, while the grain size of SC-derived phases is on the nanoscale (500−900 nm in diameter). The SEM image of the SSR compounds suggests a compact sintering between the grains due to a longer sintering process at higher temperatures. In contrast, the submicrometer-sized SC grains are particularly interconnected with channels running randomly between the sintered particles. This specific morphology can be explained by the evaporation of the solvent creating pores and channels during the decomposition of the polymeric citrate precursors. Hence, the SC compounds still reveal a three times larger specific surface area compared to the SSR phases after sintering at similar temperatures ($T >$ 1473 K). Good mechanical properties of the pellets are important criteria for the thermoelectric converters. The sintered pellets from products of the SC and SSR synthesis route present good mechanical properties. Both series of pellets sustain an applied pressure of 3 kN under operation without showing cracks.[47]

Several crystallites were studied by TEM in order to analyze locally their microstructure. The inset in Figure 3a shows a typical SC crystallite of ≃250 nm in length. The $CaMn_{0.98}Nb_{0.02}O_3$ HRTEM image (Figure 3a) shows lattice fringes corresponding to the $[100]_o$ zone axis, in the orthorhombic structure. The studied material exhibits good crystallinity without defects or dislocations. The ED pattern of the same crystallite fits well with the orthorhombic extinctions, as concluded from the structural Rietveld refinements. A second type of interesting microstructure is observed in the studied perovskite-type manganate phases. The $CaMn_{0.95}Nb_{0.05}O_3$ HRTEM images (Figure 4a and b) illustrate this additional characteristic microstructure. ED patterns of each domain A, B, and C were simulated by a Digital Micrograph 3.8.2 Gatan in fast Fourier transformed (FFT) mode. The FFTs from areas A and B correspond to twinned domains oriented along two different *b* axis orientations, that is, $[-101]_o$ and $[0-10]_o$. The FFT in region C indicates the superposition of the twinned domains. The detail in Figure 4b highlights the orientation of twinned domains, where the *b* axis is either oriented in the plane (region A) or out of the plane (region B). The presence of twinned domains suggests a certain flexibility of the crystal structure. Such twinning in the orthorhombic system is due to close lattice parameter values between the *a* and *c* axes.[14,48] Thus, the microstructure of the synthesized manganate phases is a combination of vast ordered crystalline regions and individual twinned domains as microstructural features.

(47) Tomes, P.; Trottmann, M.; Bocher, L.; Robert, R.; Hack, E.; Aguirre, M. H.; Logvinovich, D.; Shkabko, A.; Toggweiler, S.; Bitschi, A.; Hejtmanek, J.; Weidenkaff, A. Submitted for publication.
(48) Aguirre, M. H.; Robert, R.; Logvinovich, D.; Weidenkaff, A. *Inorg. Chem.* **2007**, *46*, 2744–2750.

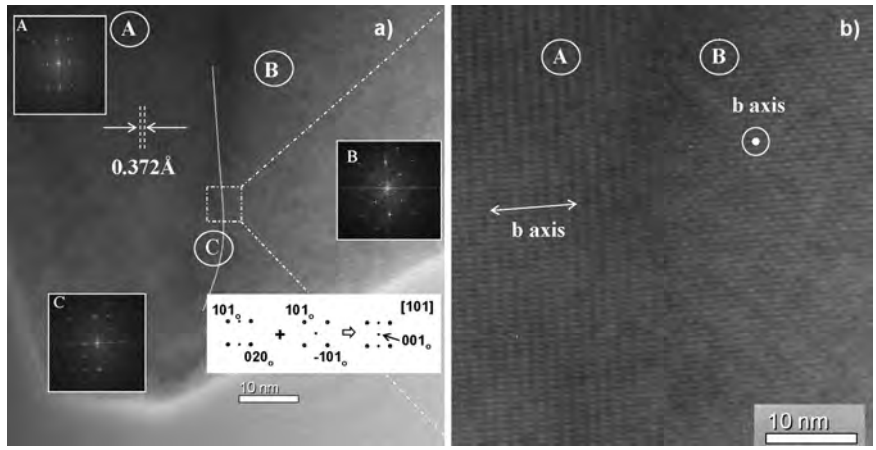

Figure 4. (a) HRTEM image of twinned domains in $CaMn_{0.95}Nb_{0.05}O_3$ (prepared by SC synthesis) in the $[101]_o$ zone axis and (b) detail of the border area between the two domains A and B. The inset figures present the fast Fourier transform (FFT) of the twinned domain A and B and the superposition of both in region C.

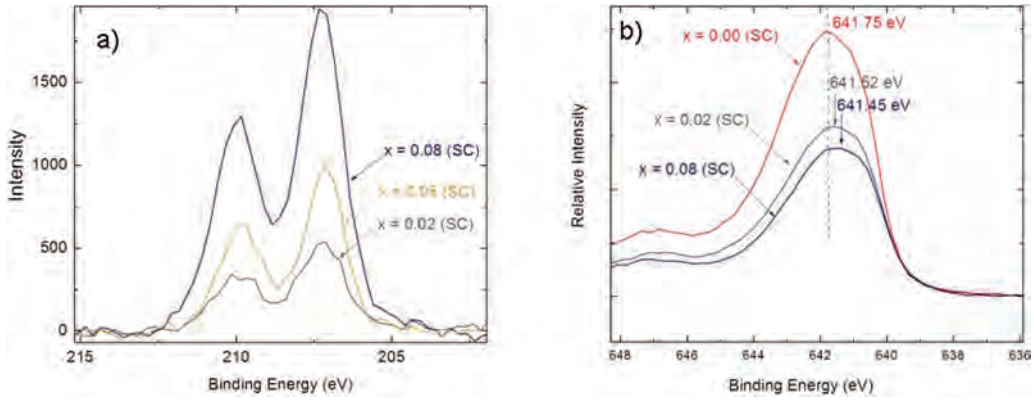

Figure 5. XPS spectra of (a) Nb $3d_{5/2}$ and (b) Mn $2p_{3/2}$ peaks of $CaMn_{1-x}Nb_xO_3$ (for $x = 0$, 0.02, 0.05, and 0.08) synthesized by a SC method.

The average Mn oxidation state was evaluated by XPS measurements and depends on the Nb substitution. The Nb 3d spectra of the sintered SC compounds show that the peak intensities increase with increasing x values (Figure 5a). The binding energies are all assigned to the $3d_{5/2}$ peak at 207.2 eV, corresponding to the Nb^{5+} state.[42] Figure 5b displays the energy shift of the Mn $2p_{3/2}$ peak. The peak position for $CaMnO_3$ (641.75 eV) is consistent with the binding energy of the Mn^{4+} oxidation state.[49] The Nb-containing phases exhibit a chemical shift to lower energy values (Mn $2p_{3/2}$ = 641.52 eV for $x = 0.02$ and Mn $2p_{3/2}$ = 641.45 eV for x = 0.08), confirming the Mn^{3+} formation in the Mn^{4+} sublattice with increasing x.

As previously reported, at low temperatures ($T < 200$ K), the resistivity for the $CaMn_{1-x}Nb_xO_3$ series ($x \leq 0.08$) increases with decreasing temperature, indicating semiconducting properties ($d\rho/dT < 0$).[14,32] The electrical transport properties change gradually with the temperature. At higher temperatures (200 K $< T <$ 1070 K), the electrical resistivity of both the SSR and the SC compounds drops to values as low as those characteristic for metals, for example, for the SC phases: for $x = 0.05$, $\rho_{400K} = 12.1$ mΩ cm. Figure 6a displays the electrical resistivity versus the temperature for all of the compounds within the range of 320 K $< T <$ 1070 K. As mentioned above, the introduction of a pentavalent cation such as Nb^{5+} generates Mn^{3+} ($e_g^1t_{2g}^3$) cations in the Mn^{4+} ($e_g^0t_{2g}^3$) matrix. Electrons in the e_g orbitals act as charge carriers in the $Mn^{4+}-O-Mn^{3+}$ ion framework. The band structure and the carrier concentration vary with the extent of Nb substitution. The transport of charge carriers in manganate phases is generally well described by the small polaron hopping model;[8,17] that is, the formation of polarons is defined as the combination of carriers with its strain field.[11] Thus, the resistivity decreases with increasing charge carrier concentration, for example, for the SSR phases from ρ_{500K} = 26 m Ω cm for $x = 0.02$ to ρ_{500K} = 11.3 m Ω cm for x = 0.08.

For equivalent Nb substitution, the SC and SSR phases present similar electrical resistivity values (for $x = 0.02$ at 800 K, $\rho = 37.7$ mΩ cm for the SSR compound and ρ = 32.4 mΩ cm for the SC compound) even if the SC phases reveal lower relative densities compared to the SSR compounds. This finding indicates that the SC phases present a better intrinsic electrical conduction than the SSR phases. The different morphologies and the size of crystallites obtained by the two synthesis methods can be considered to explain this. The SC-derived phases reveal a 6−10 times smaller grain size than the SSR compounds and a specific surface area at least twice as high as the SSR compounds. Therefore, the contact surface between different crystallites is larger in the case of the SC compounds compared to SSR

(49) Zampieri, G. *Solid State Commun.* **2002**, *123*, 81–85.

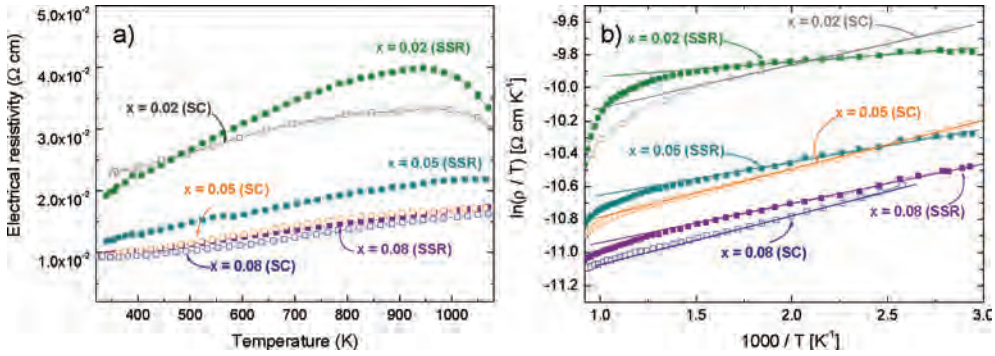

Figure 6. Temperature dependence of the resistivity and for $CaMn_{1-x}Nb_xO_3$ (for $x = 0.02$, 0.05, and 0.08) synthesized by SSR (closed symbols) and SC methods (open symbols). *Results match with data from a previous work.[14]

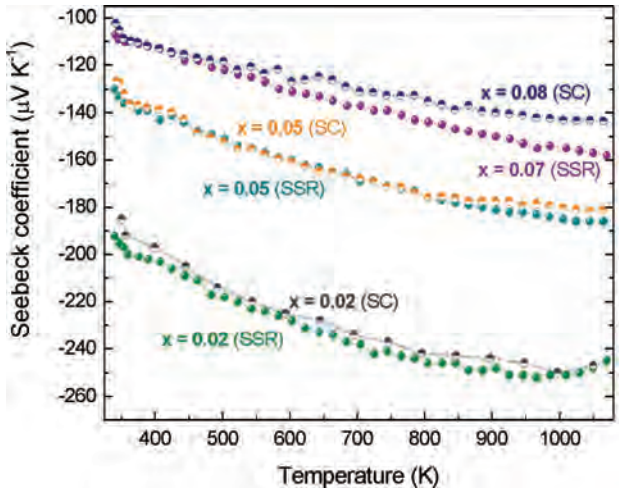

Figure 7. Temperature dependence of Seebeck coefficients for $CaMn_{1-x}Nb_xO_3$ (for $x = 0.02$, 0.05, and 0.08) synthesized by both a SSR (closed symbols) and a SC (half-open symbols) method. Results match with data from a previous work.[14]

phases. The SC phases present a particular morphology with good interconnections between the crystallites, promoting the transport of charge carriers.

Thermogravimetric analyses were performed to confirm the thermal stability of all of the compounds in the studied temperature range. All compounds present large negative thermopower values, that is, $|S| > 100$ μV K^{-1}, in the temperature range from 300 to 1070 K (Figure 7), indicating that electrons are the predominant charge carriers. Identical thermopower values and $S(T)$ behavior are measured for the compounds with equivalent Nb content irrespective of the synthesis method. This confirms that the different microstructures of the SSR and SC phases do not influence either the charge carrier concentration or the electronic band structure. The sole exception is the SSR compound with 8% Nb having a slightly higher absolute thermopower value at $T > 500$ K compared to the corresponding SC compound. The analysis of the cationic composition reveals a small Nb deficiency for the SSR phase ($x = 0.069 \pm 0.020$) in comparison to the expected composition, suggesting a higher Mn^{4+} concentration associated with a larger $|S|$ value. Moreover, the charge carrier concentration can be determined from the experimental thermopower values by applying the Heikes formula.[51] The Heikes formula states that the thermopower should tend to $S_{Heikes} = -k_B/|e| \ln (1 - x)/x$ in the high-temperature limit (where k_B is the Boltzmann constant and x is the charge carrier concentration). Thus, the 8% SSR compound presents an $S_{1050K} = -157$ μV K^{-1}, corresponding to 13.8% Mn^{3+} cations, while the 8% SC-derived phase shows an $S_{1045K} = -143$ μV K^{-1} equal to 15.9% Mn^{3+} cations. The 2% Nb phases present a change of electrical resistivity and thermopower behavior above 1000 K, probably related to a high-temperature structural transition.[52] Thus, the Heikes law is not valid for the $CaMn_{0.98}Nb_{0.02}O_3$ phase at $T > 1000$ K.

Increasing the Nb content in the Mn sublattice leads to a decrease in absolute Seebeck coefficients from $S_{900K} = -248$ μV K^{-1} for $x = 0.02$ to $S_{900K} = -150$ μV K^{-1} for $x = 0.08$ following the Heikes law at high temperatures. This is explained by an increase in the charge carrier concentration inducing a decrease in the electrical resistivity. The largest Seebeck coefficients are obtained for both SSR and SC compounds with 2% Nb substitution ($S_{1000K} = -251$ μV K^{-1}). As a general tendency, the Seebeck coefficient exhibits a linear temperature dependence in the paramagnetic region; that is, $|S|$ values increase with increasing temperature. The metal-like electrical resistivity and linear $S(T)$ behavior of the $CaMn_{1-x}Nb_xO_3$ series allows application of the modified expression of the thermopower single band metal: $S_{theo} = [(-\pi^2 k_B^2)/(3e)]T[N(E)/n + cst]_{E=Ef}$ (where $N(E)$ is the density of states and n is the carrier density), as previously reported for other electron-doped manganate phases.[8,17,22] Thus, theoretical Seebeck coefficients can be determined at 300 K for a defined Nb content and compared with the experimental values (e.g., for $x = 0.05$, $S_{theo} = -130$ μV K^{-1} and $S_{exp} = -128$ μV K^{-1} at 340 K).

The same thermopower values for compounds with equal Nb content are observed, no matter which synthesis process was applied. This result confirms the high quality/purity of the compounds, since the Seebeck coefficient depends on the electronic band structure of the material. However, the SC samples reveal lower resistivity values due to a better

(50) Hébert, S.; Martin, C.; Maignan, A.; Hejtmanek, J.; Raveau, B. *Proc. 6th European Workshop on Thermoelectrics*; IPM Freiburg: Germany, 2001.
(51) Heikes, R. R.; Ure, R. W. *Thermoelectricity: Science and Engineering*; Interscience: New York, 1961.
(52) Taguchi, H.; Nagao, M.; Stao, T.; Shimada, M. *J. Solid State Chem.* **1989**, *78*, 312–315.

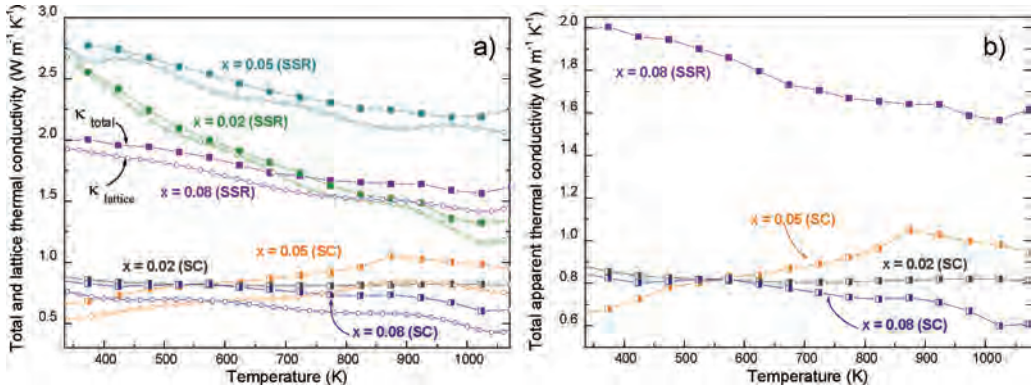

Figure 8. (a) Total thermal conductivity κ_{total} of $CaMn_{1-x}Nb_xO_3$ ($x = 0.02$, 0.05, and 0.08) synthesized by both SSR (closed symbols) and SC (half-open symbols) methods and lattice contribution κ_l (open symbols) versus T and (b) highlight in the low thermal conductivity range.

Table 4. Relative Bulk Density and Electrical Resistivity Values Depending on the Extent of Nb Substitution and the Synthesis Method for the $CaMn_{1-x}Nb_xO_3$ Series[a]

niobium substitution	Mn valency	synthesis method	relative density	ρ (mΩ cm) at 800 K
0.02	3.98	SSR	86.01%	37.7
		SC	80.77%	32.4
0.05	3.94	SSR	82.74%	19.5
		SC	67.79%	15.6
0.08	3.91	SSR	78.12%	14.8
		SC	72.25%	13.7

[a] Mn valency determined according to the expected composition $CaMn_{1-x}Nb_xO_3$.

interconnection between the crystallites, resulting in a higher power factor (PF). The largest power factor is achieved for the $CaMn_{0.95}Nb_{0.05}O_3$ SC phase, ranging from $PF_{450K} = 1.92 \times 10^{-4}$ W m^{-2} K^{-1} to $PF_{1050K} = 2.02 \times 10^{-4}$ W m^{-2} K^{-1}.

Figure 8a displays the total thermal conductivity and the lattice contribution (340 K $< T <$ 1070 K) for all of the studied compounds. The electronic component, κ_e, can be estimated from the electrical resistivity data using the Wiedemann−Franz law ($\kappa_e = L_oT\sigma$, where $L_o = 2.45 \times 10^{-8}$ W Ω K^{-2} is the Lorenz number and σ is the electrical conductivity). The calculated κ_e, the thermal diffusivity, and conductivity values at 800 K are summarized in Table 5. Since κ_e does not exceed 20% of the total thermal conductivity, heat conduction is predominantly represented by the lattice component, κ_l. In addition, the electronic thermal conductivity depends both on the temperature and on the carrier concentration. Thus, increasing the Nb substitution results in an increase of the electronic contribution, κ_e (e.g., for the SSR phases at 800 K, from $\kappa_e = 4.20\%$ for $x = 0.02$ to $\kappa_e = 8.03\%$ for $x = 0.08$).

As for the SSR compounds, the total heat conductivity, κ_{total}, shows a common temperature dependence, that is, κ_{total} decreases slightly with increasing temperature. This behavior does not apply for the SC phases and might be related to generally lower thermal conductivities of SC compounds ($\kappa_{total} < 1$ W m^{-1} K^{-1}) compared to the SSR phases (1.5 W m^{-1} K^{-1} $< \kappa_{total} <$ 3.0 W m^{-1} K^{-1}), which show typical values for oxide materials.[21,53] However, a direct comparison of the κ_{total} values is not possible, since SSR and SC phases differ in relative densities (78−86% and 67−80%, respectively). Therefore, values have to be related to a 100% dense material using the Maxwell relation,[13,54] $\kappa_{dense} = \kappa_{measured}/(1 - 1.5\phi)$, where ϕ accounts for the volume porosity, assuming spherical pores. These evaluations are considered as first approximation since the SC compounds present a heterogeneous shape of the pores. Calculation results are presented in Table 5, revealing higher κ_{dense} values for the SSR compounds compared to the SC phases. In addition, the SC phases have lower thermal diffusivity values compared to the SSR compounds ($\alpha_{SSR} \simeq 0.60$ mm^2 s^{-1} and $\alpha_{SC} \simeq 0.32$ mm^2 s^{-1} at 800 K). This finding confirms that the lower κ values for the SC compounds do not result from the different relative density since the thermal diffusivity is not related to the relative density. Another possibility to clarify the low thermal conductivity values is the effect of the size of twinned domains on the phonon scattering. The occurrence of twinned domains, shown by the HRTEM image in the SC phases, can be explained crystallographically. In comparison, twinned domains could be also identified in the SSR series by ED patterns. However, the size of the SC crystallites is smaller (200 nm diameter) than that of the SSR crystallites (in the micrometer range), leading to twinned domains of different dimensions. Lower thermal conductivity values, implying higher phonon scattering in SC phases, might result from the nanosized twinned domains or the porous morphology.

Figure 9 presents the dimensionless figure of merit, ZT, of the studied compounds within the temperature range of 340 K $< T <$ 1070 K. Large power factors are achieved at low Nb substitution levels. The SSR compounds present a maximum ZT value for $CaMn_{0.98}Nb_{0.02}O_3$ with $ZT_{1060K} = 0.16$, while for the SC series, a ZT value twice as high is obtained for the same composition (2% Nb) with $ZT_{1060K} = 0.32$. A previous work reported a ZT value of 0.37 at 1000 K for heterostructures of Nb-doped $SrTiO_3$ epitaxial thin films.[55] Thus, the present result belongs to one of the best ZT values measured in *n*-type polycrystalline oxide materials, where the highest value reported ($ZT_{1073K} = 0.33$) was determined for Y-doped In_2O_3−ZnO.[54] Thus, the electron-doped manganate phases appear as potential *n*-type legs for

(53) Clarke, D. R. *Surf. Coat. Technol.* **2003**, *67*, 163–164.
(54) Schliting, K. W.; Padture, N. P.; Klemens, P. G. *J. Mater. Sci.* **2001**, *36*, 3003–3010.
(55) Ohta, S.; Nomura, T.; Ohta, H.; Hirano, M.; Hosono, H.; Koumoto, K. *Appl. Phys. Lett.* **2005**, *87*, 092108.

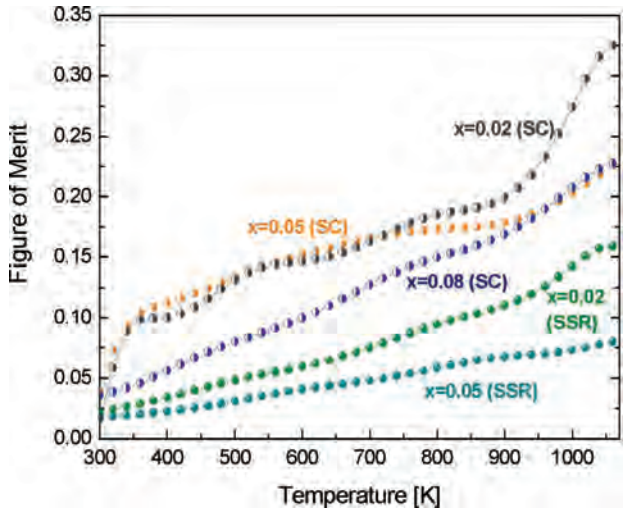

Figure 9. Temperature dependence of the figure of merit for $CaMn_{1-x}Nb_xO_3$ (for $x = 0.02$, 0.05, and 0.08) synthesized by both SSR (closed symbols) and SC (open symbols) methods.

the development of a thermoelectric oxide module and therefore to evaluate the output power and the conversion efficiency of the thermoelectric converter.[47]

Conclusions

This study shows that the morphology of single-phase $CaMn_{1-x}Nb_xO_{3\pm\delta}$ ($x = 0.02$, 0.05, and 0.08) perovskite-type compounds can differ dramatically by applying either the standard SSR method or the SC synthesis route. The SSR-derived phases present typical sintered micrometer-size grains, leading to a compact and dense structure. The SC synthesis route is based on the decomposition of complex polymeric precursors where the cations are homogenously premixed in aqueous solution. Hence, low-level substitutions can be better controlled. Another advantage of the SC synthesis route originates from the decomposition of the polymeric precursors, leading to submicrometer-size sintered grains interconnected in a particular way. The phase formation occurs at relatively low temperatures ($T < 1073$ K) since no diffusion processes are necessary, unlike in the SSR method. Therefore, larger surface area materials are achieved by the SC method, avoiding time-consuming sintering conditions compared to the SSR synthesis route.

The crystal structure of the synthesized compounds belongs to the orthorhombic *Pnma* space group, confirmed by Rietveld refinements of the ND data. The structural characterization reveals an increase of the lattice and cell parameters with increasing Nb substitution and an enhancement of the orthorhombic distortion. The TEM study highlights a complex microstructure where twinned domains

Table 5. Total Thermal Conductivity, κ_{total}, Electronic Contribution, κ_e, Dense Thermal Conductivity, κ_{dense}, and Thermal Diffusivity, α, at 800 K for the $CaMn_{1-x}Nb_xO_3$ ($x = 0.02$, 0.05, 0.08) Synthesized by Both a SSR and a SC Method

niobium substitution	synthesis method	κ_{total} (W m^{-1} K^{-1})	κ_e (%)	κ_{dense} (W m^{-1} K^{-1})	α (mm^2 s^{-1})
0.02	SSR	1.53	4.20	2.17	0.336
	SC	0.78	7.78	1.06	0.585
0.05	SSR	2.27	4.63	3.05	0.303
	SC	0.91	13.93	1.76	0.688
0.08	SSR	1.66	8.03	2.12	0.341
	SC	0.73	19.57	1.11	0.542

are combined with long-range ordered crystalline regions. Close lattice parameters, such as $a \sim c \sim b/\sqrt{2} \sim a_p\sqrt{2}$, are responsible for such twinning of the crystal structure.

The differences in morphology/microstructure influence the transport properties. The SSR and SC phases yield to equal Seebeck coefficients for the same Nb substitution level since the thermopower depends on electronic band structure and charge carrier concentrations. The electrical resistivities of both series follow a metallic-like behavior. However, the SC phases reveal lower intrinsic electrical resistivity than the SSR compounds, probably due to the better surface contact between the SC crystallites. The SC phases exhibit thermal conductivity values below 1 W m^{-1} K^{-1}, which is considerably lower than for the SSR-derived phases. The major contribution to the thermal conductivity, in the studied phases, originates from the lattice component ($\kappa_{lattice} > (80-95\%)\ \kappa_{total}$); that is, the heat conduction in oxide materials is generally dominated by the motion of phonons. Introducing nanosized twinned domains in the SC phases can act as scattering centers effective for the phonons but ineffective for the charge carriers. The enhancement of phonon scattering in the SC phases can be explained in terms of the size of twinned domains in the microstructure or the porous morphology. The results lead to high ZT values for the SC phases, that is, $ZT_{1060K} = 0.32$ for the 2% Nb, twice as high compared to the standard SSR phases. The achieved TE material is a prospective *n*-type thermoelement able to operate in the air at high temperatures.

Acknowledgment. The authors would like to thank the Swiss Federal Office of Energy (BfE) and Empa for the financial support. The neutron experiments were performed at the Swiss Spallation Neutron Source SINQ, Paul Scherrer Institute, Villigen Switzerland. The authors thank P. Hug for the helpful assistance with the LFA measurements as well as D. Sheptyakov and S. Ebbinghaus for their support with the neutron measurements campaign and both S. Hébert and A. Maignan for the fruitful discussions.

IC800463S